Journal of
Mechanics of
Materials and Structures

ANALYTICAL MODELING AND COMPUTATIONAL ANALYSIS ON TOPOLOGICAL PROPERTIES OF 1-D PHONONIC CRYSTALS IN ELASTIC MEDIA

Muhammad and C. W. Lim

Volume 15, No. 1 January 2020

msp

JOURNAL OF MECHANICS OF MATERIALS AND STRUCTURES
Vol. 15, No. 1, 2020
dx.doi.org/10.2140/jomms.2020.15.15

ANALYTICAL MODELING AND COMPUTATIONAL ANALYSIS ON TOPOLOGICAL PROPERTIES OF 1-D PHONONIC CRYSTALS IN ELASTIC MEDIA

MUHAMMAD AND C. W. LIM

The topological interface state governed by topological phononic crystals (PnC) can potentially host one-way, backscattering free nontrivial edge modes, immune to defects and sharp edges. We study here 1D topological phononic crystals with interface modes/states generated by an exchange of wave mode polarization and geometric phases, using the spectral element method with Timoshenko beam model for flexural wave propagation. The constitutive relations for the longitudinal wave, and modeling and formulation are derived for theoretical band structure and frequency response studies. The analysis is validated by finite element numerical simulations. The geometric phases of the Bloch bands are determined by numerical Zak phase analysis. As the geometric properties of the PnC vary, a band transition resulting from an exchange in wave mode polarization is observed and the symmetry characteristics of the Bloch bands are determined. The geometric phases provide useful information about the interface mode that is generated when the mode transition frequency is common between the bandgaps of topological PnC. We further conduct theoretical and numerical studies on the presence of interface state and excellent agreement observed between both models is reported. The theoretical details of the topological PnC with protected interface mode can be helpful for better understating of research in phononic crystals.

A list of symbols can be found on page 32.

1. Introduction

Recent advances in the study of the quantum Hall effect [Haldane 1988], valley Hall effect [Dong et al. 2017; Zhou et al. 2019a] and quantum spin Hall effect [Bernevig et al. 2006; Kane and Mele 2005] in classical wave physics have paved the way for novel discoveries in the photonic and phononic research community. Analogous to the quantum theory presented, physicists explored the realm of periodic structures in solids supported by theory [Kushwaha et al. 1993; Sigalas and Economou 1993], observation [Martínez-Sala et al. 1995] and experimental work [Liu et al. 2000]; those authors investigated the propagation of acoustic and elastic waves in a periodic array of scatterers that revealed frequency bandgap characteristics where no wave propagation occurs. The discovery of topological insulators [Hasan and Kane 2010; Huber 2016; Moore 2010], which exhibit topological properties with nontrivial geometric phases in the electronic system and counterpart photonic [Khanikaev et al. 2013] and phononic crystals (PnCs) in both acoustic [Xiao et al. 2015; Zhao et al. 2018] and elastic [Muhammad et al. 2019; Zhou et al. 2019b] media has opened up an active research area for the study of new physical phenomena related

Muhammad's ORCID is 0000-0003-3492-0123.

Keywords: geometric phase, interface mode, spectral element, topological phononic crystals, Zak phase, geometric phase, interface mode, spectral element, topological phononic crystals, Zak phase.

to topological phases. Topology as a tool has been recently explored in conventional band theories and marvelous wave characteristics in hexagonal lattices [Chen et al. 2018b; Chen et al. 2018a; Jia et al. 2018; Khanikaev et al. 2015; Pal et al. 2018; Reda et al. 2016; Xia et al. 2018], beams [Kim et al. 2018; Li et al. 2018; Muhammad et al. 2019; Zhou et al. 2019b] and plate structures [Brendel et al. 2018; Foehr et al. 2018; Jin et al. 2018; Miniaci et al. 2018] have been reported.

Spatially, the topological properties illustrate the quantized behavior of the wavefunctions over an associated band structure and they greatly influence the transportation behavior of phonons and photons. Furthermore, they also preserve certain symmetry against the local perturbation and the symmetric properties are retained unless the perturbation is not strong enough to close the bandgap of topological PnCs [Ma et al. 2019]. The topological characteristics is governed either by actively breaking time reversal symmetry, mimicking the quantum Hall effect [Haldane 1988; Mei et al. 2016] or nucleation and coupling of degenerate modes [Cha and Daraio 2018; Miniaci et al. 2018; Susstrunk and Huber 2015], and analogues to the quantum spin Hall effect. They are demonstrated through the Dirac cone dispersion plot. The peculiar characteristics of the topologically distinct PnCs include the generation of topologically protected interface mode (TPIM) at the junction of topologically protected unit cells. The primary characteristics of TPIM include robustness and backscattering immune single way wave transport without any loss of energy. Furthermore, TPIMs have a maximum amount of energy that concentrates at the interface of topological PnCs with decaying energy fields away from it. Such TPIMs can also control, divert, confine and enhance the propagation of elastic waves in solid structures [Miniaci et al. 2018; Muhammad et al. 2019; Xia et al. 2018; Zhang et al. 2019]. The recently proposed idea of reprogrammable TPIMs in acoustic [Xia et al. 2018] and elastic media [Zhang et al. 2019; Zhou et al. 2019a; Zhou et al. 2019c] is also intriguing. These modes also govern different characteristics with reference to passband and bandgap frequencies as explained by [Muhammad et al. 2019]. Nonlinear nanobeam vibration with surface effects [Chen et al. 2019a], auxetic metamaterials [Andrade et al. 2018] and topological optimization of spatially continuum structure [Czubacki et al. 2015] has also been reported.

The geometric phases of Bloch bands are determined by topological invariants such as Zak phase [Delplace et al. 2011; Muhammad et al. 2019; Xiao et al. 2015; Zhou et al. 2019b] or Berry phase [Chen et al. 2019b; Wang et al. 2015; Xiao et al. 2010] for 1D and 2D PnCs respectively. For the details of theoretical and experimental observation of the Zak phase, one may refer to [Xiao et al. 2015]. The Zak phase provides information about the symmetry characteristics of Bloch bands and help distinguish the symmetric and unsymmetric edge modes of topological PnCs that further helps in the derivation of TPIMs. A detailed analysis on the geometric phases is given in Section 4. As is today, the reported works like one-way elastic edge state [Wang et al. 2015; Yu et al. 2018], topological valley transport [Huo et al. 2017; Zhang et al. 2013; Zhang et al. 2019], helical edge modes [Miniaci et al. 2018; Susstrunk and Huber 2015] and topological insulators [He et al. 2016; Huber 2016; Yu et al. 2018] etc are well recognized. Although multiple studies have investigated topological properties in photonics, electromagnetic and acoustic systems yet due to complex medium characteristics, the propagation of elastic waves in solids is still an open challenge. Furthermore, as already explored for the other wave media, TPIM in an elastic system may have more far-reaching applications in engineering vibration problems in civil, mechanical and aerospace engineering.

The present study extends and generalizes the reported work of [Muhammad et al. 2019] with a more generalize Timoshenko beam model to investigate the topological characteristics of 1D PnC beam. Using

the spectral element method, the dispersion relation and frequency response spectra for the longitudinal and bending elastic waves are established. In this study, a commercial finite element method (FEM) simulation code COMSOL Multiphysics is applied to validate the theoretical research findings and both theoretical and numerical results do show excellent agreement. A 1D PnC with varying cross-sectional area is proposed and the geometric phases of the Bloch band is determined by analyzing the Zak phase. The symmetry characteristics of the edge modes are determined and through the Dirac cone dispersion analysis the band transition and exchange in wave mode polarization are studied. The Dirac cone for the longitudinal wave is related to a symmetric band inversion as compared to bending waves where unsymmetric band transition due to nonlinear wave dispersion behavior is observed [Muhammad et al. 2019]. Two topologically distinct PnCs with different edge modes symmetry characteristic induces an interface mode provided that the mode transition frequency (band transition point) is present inside the bandgap of topological PnCs. We also perform a study on the finite unit cell based frequency response to reveal the existence of TPIM by both theoretical and numerical analyses. This theoretical and numerical model may help phononic community to better understand the physical phenomenon. The robustness with confinement of the wave energy at the interface of PnCs can be useful for solving vibration related engineering problems.

The paper is organized as follow. The topological beam model is explained in Section 2. Section 3 develops the theoretical formulation for a finite and an infinite unit cell model. Numerical formulation and Zak phase are explained in Section 4. The results are discussed in Section 5, and Section 6 presents conclusions.

2. Problem definition and physical modeling

A thick beam model as illustrated in Figure 1 is considered here. The model consists of a piecewise continuous periodic circular beam with two thinner sections sandwiching a thicker section. The lattice length of the periodic structure is a and L_A, D_A are length and diameter of the thicker beam while, L_B, d_B designate the length and diameter of the thinner beam. The material properties and geometric parameters are as follows:

$$L = 40\,\text{mm}; \quad D_A = 8\,\text{mm}; \quad d_B = 4\,\text{mm}; \quad \text{density } \rho = 2700\,\text{kg/m}^3;$$
$$\text{Young's modulus } E = 70\,\text{GPa}; \quad \text{Posson's ratio } \nu = 0.33.$$

In general, for any elastic beam structure, longitudinal and bending waves coexist with distinct wave dispersion characteristic. The propagation of longitudinal waves is linearly dispersive that is governed by $\omega^2 = k^2 E/\rho$, however, flexural waves show nonlinear dispersion behavior. To ensure the decoupling of longitudinal and flexural waves, the unit cell of the PnC is arranged symmetrically with respect to the xy-plane. A topological shape parameter $\delta = (L_A + 2L_B)/L$ is introduced to characterize a topologically distinct unit cell.

The spectral element method with Timoshenko beam model is applied here to derive the band structure and frequency response spectra for bending waves. A constitutive relation for dispersion spectra of longitudinal wave is also derived (see Section 3.1). The symmetry properties of the edge modes are determined by the Zak phase (see Section 4). The theoretical findings are validated by numerical simulations of COMSOL Multiphysics.

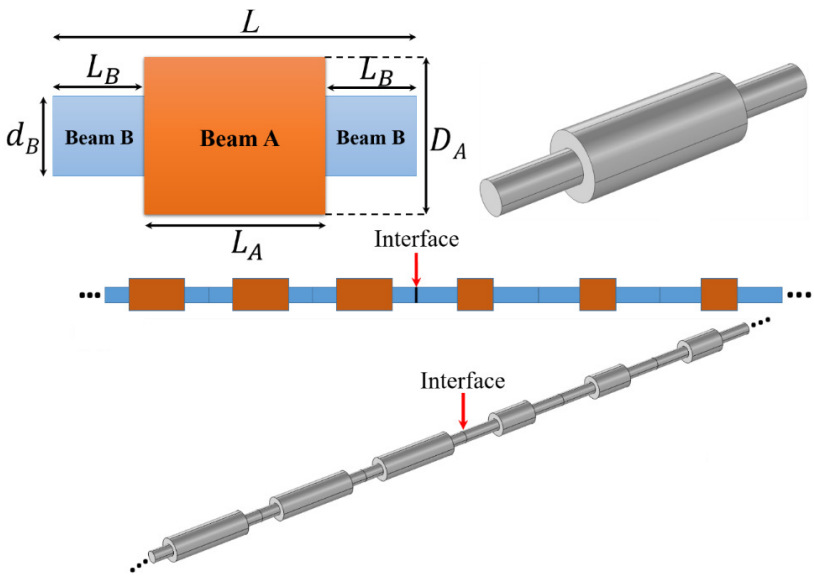

Figure 1. Top: geometry of the PnC beam units. Bottom: finite length PnC beam with interface highlighted by red arrows.

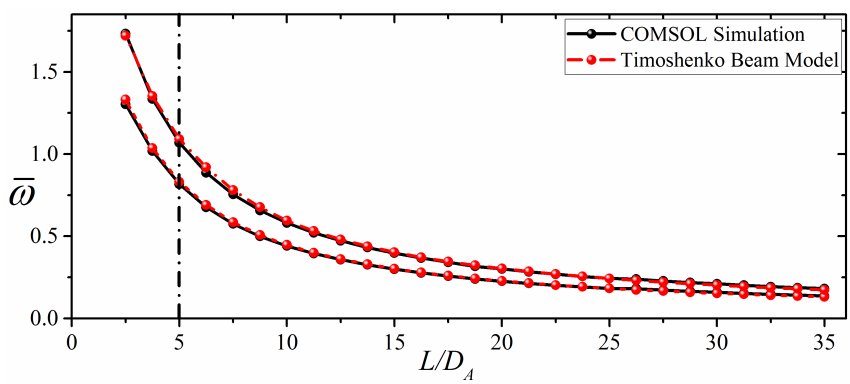

Figure 2. Comparison of the theoretical and numerical models for flexural wave propagation with varying slenderness ratio L/D_A. Black dashed line for $L/D_A = 5$ represents geometric parameter adopted in the present study.

3. Governing equations and solution methodology

3.1. ***Flexural waves.*** For flexural wave propagation in a beam with a considerable thickness-to-length ratio (significantly shear deformable), the characteristic equation of motion can be expressed as follows [Gao et al. 2018; Yu et al. 2006; Zhou et al. 2019b]:

$$\frac{EI_z}{\rho S}\frac{\partial^4 w(x,t)}{\partial x^4} - \frac{I_z}{S}\left(1+\frac{E}{\kappa G}\right)\frac{\partial^4 w(x,t)}{\partial x^2 \partial t^2} + \frac{\partial^2 w(x,t)}{\partial t^2} + \frac{\rho I_z}{\kappa G S}\frac{\partial^4 w(x,t)}{\partial t^4} = 0, \tag{1}$$

where EI_z, G and κ are flexural rigidity, shear modulus and shear correction factor for the beam, while S, ρ are cross-sectional area, mass density and $w(x,t) = W(x)e^{i\omega t}$ is lateral displacement of the beam with $W(x)$ being mode shape function and ω is angular frequency. For a circular or rectangular beam, the following expressions apply:

$$I_z = \begin{cases} \dfrac{wh^3}{12} & \text{(rectang.)} \\ \dfrac{\pi D^4}{64} & \text{(circular)} \end{cases} \qquad EI_z = \begin{cases} \dfrac{Ewh^3}{12} & \text{(rectang.)} \\ \dfrac{\pi E D^4}{64} & \text{(circular)} \end{cases} \qquad \kappa = \begin{cases} \dfrac{5(1+\nu)}{6+5\nu} & \text{(rectang.)} \\ \dfrac{6(1+\nu)^2}{7+12\nu+4\nu^2} & \text{(circular)} \end{cases} \tag{2}$$

For such a shear deformable beam, the Timoshenko beam model is applicable. The governing equation for bending moment and shear force is, respectively,

$$M = EI_z \frac{\partial \psi}{\partial x}, \quad V = \kappa GS\left(\frac{\partial w}{\partial x} - \psi\right), \tag{3}$$

where ψ is the angular rotation of circular beam that is related to $w(x)$ by

$$\psi = \frac{EI_z}{\kappa GS - \rho I_z \omega^2}\frac{\partial^3 w(x)}{\partial x^3} + \frac{1}{\kappa GS - \rho I_z \omega^2}\left(EI\frac{\rho}{\kappa G}\omega^2 + \kappa GS\right)\frac{\partial w(x)}{\partial x}. \tag{4}$$

For generality in formulation, the key quantities are made dimensionless by introducing the variables

$$\begin{gathered} \bar{w} = w/L, \quad \bar{x} = x/L, \quad \overline{\omega} = \omega L\sqrt{\rho_B/E_B} \quad \phi = EI_z/(E_B L^4), \bar{\rho} = \rho/\rho_B, \\ \bar{S} = S/L^2, \quad \bar{I}_z = I_z/L^4, \quad \overline{G} = G/E_B, \quad \overline{M} = M/(E_B L^3), \quad \overline{V} = V/(E_B L^2), \end{gathered} \tag{5}$$

where E_B and ρ_B are Young's modulus and density of beam B, respectively. By substituting (4) into (3), the normalized constitutive relations are

$$\psi = A\bar{w}''' + B\bar{w}', \quad \overline{M} = C\bar{w}''(\bar{x}) + Dw(\bar{x}),, \quad \overline{V} = \kappa\overline{G}\bar{S}((1-B)\bar{w}' - A\bar{w}'''). \tag{6}$$

The normalized bending moment using (6) becomes

$$\psi'(\bar{x}) = \bar{w}''(\bar{x}) + \frac{\overline{\rho\omega}^2}{\kappa\overline{G}}\bar{w}. \tag{7}$$

In (6) and (7)) the derivatives are with respect to $\bar{x}$ and A, B, C, D are given by

$$A = \frac{\phi}{\kappa\overline{G}\bar{S} - \bar{\rho}\bar{I}_z\overline{\omega}^2}, \quad B = \frac{1}{\kappa\overline{G}\bar{S} - \overline{\rho}\bar{I}_z\overline{\omega}^2}\left(\phi\frac{\bar{\rho}}{\kappa\overline{G}}\overline{\omega}^2 + \kappa\overline{G}\bar{S}\right), \quad C = \phi, \quad D = \phi\frac{\bar{\rho}\overline{\omega}^2}{\kappa\overline{G}}. \tag{8}$$

Using these dimensionless quantities, (1) can be rewritten as

$$\phi\frac{\partial^4\bar{w}}{\partial\bar{x}^4} + \left[\left(\frac{\phi}{\kappa\overline{G}} + \bar{I}_z\right)\bar{\rho}\overline{\omega}^2\right]\frac{\partial^2}{\partial\bar{x}^2}\bar{w} - \bar{\rho}\overline{\omega}^2\left(\bar{S} - \frac{\bar{\rho}\bar{I}_z\overline{\omega}^2}{\kappa\overline{G}}\right)\bar{w} = 0. \tag{9}$$

As in [Zhou et al. 2019b], the surface effect is neglected here. The harmonic solution to (9) is

$$\bar{w}(\bar{x}) = A_1 e^{i\zeta\bar{x}}. \tag{10}$$

Substituting this relation into (9) yields

$$S_1\zeta^4 + S_2\zeta^2 + S_3 = 0, \tag{11}$$

with

$$S_1 = \phi, \quad S_2 = -\bar{\rho}\overline{\omega}^2\left(\frac{\phi}{\kappa\overline{G}} + \bar{I}_z\right), \quad S_3 = -\bar{\rho}\overline{\omega}^2\left(\bar{S} - \frac{\bar{\rho}\bar{I}_z}{\kappa\overline{G}}\overline{\omega}^2\right). \tag{12}$$

Solving (11) in ζ yields four solutions:

$$\zeta_1 = -\zeta_2 = \sqrt{\frac{-S_2 + \sqrt{S_2^2 - 4S_1S_3}}{2S_1}}, \quad \zeta_3 = -\zeta_4 = \sqrt{\frac{-S_2 - \sqrt{S_2^2 - 4S_1S_3}}{2S_1}}. \tag{13}$$

Hence, the general solution of (11) can be expressed as

$$w(\bar{x}) = A_1 e^{i\chi_1\bar{x}} + A_2 e^{i\chi_2\bar{x}} + A_3 e^{i\chi_3\bar{x}} + A_4 e^{i\chi_4\bar{x}}, \tag{14}$$

where the A_j $(j = 1, 2, 3, 4)$ are unknown coefficients to be determined by the boundary conditions.

We introduce a nodal displacement vector $\boldsymbol{q} = (\boldsymbol{q}_L^T \ \boldsymbol{q}_R^T)^T$, which according to (6) can be written as

$$\boldsymbol{q} = \boldsymbol{P}\boldsymbol{b}. \tag{15}$$

Superscript T in the equations above means transposition, $\boldsymbol{q}_L = [\bar{w}(0)\ \psi(0)]^T$, $\boldsymbol{q}_R = \left[\bar{w}(\bar{L})\psi(\bar{L})\right]^T$, $\boldsymbol{b} = [A_1\ A_2\ A_3\ A_4]^T$ and

$$\boldsymbol{P} = \begin{bmatrix} 1 & 1 & 1 & 1 \\ iX_1 & iX_2 & iX_3 & iX_4 \\ e^{i\zeta_1\bar{L}} & e^{i\zeta_2\bar{L}} & e^{i\zeta_3\bar{L}} & e^{i\zeta_4\bar{L}} \\ iX_1e^{i\zeta_1\bar{L}} & iX_2e^{i\zeta_2\bar{L}} & iX_3e^{i\zeta_3\bar{L}} & iX_4e^{i\zeta_4\bar{L}} \end{bmatrix}, \tag{16}$$

where $X_j = \zeta_j(B - A\zeta_j^2)$ and $\bar{L} = L_B/2$ or L_A. The nodal force vector $\boldsymbol{f} = \left[\boldsymbol{f}_L^T \ \ \boldsymbol{f}_R^T\right]^T$ is written as

$$\boldsymbol{f} = \boldsymbol{R}\boldsymbol{b}, \tag{17}$$

in which $\boldsymbol{f}_L = \left[-\overline{M}(0) - \overline{V}(0)\right]^T$ and $\boldsymbol{f}_R = \left[\overline{M}(\bar{L})\overline{V}(\bar{L})\right]^T$. Here $\boldsymbol{R}$ is

$$\boldsymbol{R} = \begin{bmatrix} -Z_1 & -Z_2 & -Z_3 & -Z_4 \\ -iY_1 & -iY_2 & -iY_3 & -iY_4 \\ Z_1e^{i\zeta_1\bar{L}} & Z_2e^{i\zeta_2\bar{L}} & Z_3e^{i\zeta_3\bar{L}} & Z_4e^{i\zeta_4\bar{L}} \\ iY_1e^{i\zeta_1\bar{L}} & iY_2e^{i\zeta_2\bar{L}} & iY_3e^{i\zeta_3\bar{L}} & iY_4e^{i\zeta_4\bar{L}} \end{bmatrix}, \tag{18}$$

where $Y_j = \kappa\overline{G}\bar{S}\left(1 - B + A\zeta_j^2\right)\zeta_j$, $Z_j = D - C\zeta_j^2$ with $j = 1, 2, 3, 4$. Combining (16), (17) and (18), we get

$$\begin{bmatrix} \boldsymbol{f}_L^{(A,B)} \\ \boldsymbol{f}_R^{(A,B)} \end{bmatrix} = \begin{bmatrix} \boldsymbol{D}_{LL}^{(A,B)} & \boldsymbol{D}_{LR}^{(A,B)} \\ \boldsymbol{D}_{RL}^{(A,B)} & \boldsymbol{D}_{RR}^{(A,B)} \end{bmatrix} \begin{bmatrix} \boldsymbol{q}_L^{(A,B)} \\ \boldsymbol{q}_R^{(A,B)} \end{bmatrix}. \tag{19}$$

Superscript A, B denote the parameters calculated on the left and right sides of subbeams A and B. Also, we have

$$\boldsymbol{D}^{(A,B)} = \begin{bmatrix} \boldsymbol{D}_{LL}^{(A,B)} & \boldsymbol{D}_{LR}^{(A,B)} \\ \boldsymbol{D}_{RL}^{(A,B)} & \boldsymbol{D}_{RR}^{(A,B)} \end{bmatrix} = \boldsymbol{R}^{(A,B)}\left(\boldsymbol{P}^{(A,B)}\right)^{-1}, \tag{20}$$

which is the dynamic stiffness matrix. The dispersion relation and band structure study involve an infinite periodic unit cell structure. The equation of motion for each unit cell can be described by the dynamic stiffness matrix as follows:

$$\begin{bmatrix} \boldsymbol{f}_L^B \\ \boldsymbol{f}_R^A \end{bmatrix} = \begin{bmatrix} \boldsymbol{Q}_{LL} & \boldsymbol{Q}_{LR} \\ \boldsymbol{Q}_{RL} & \boldsymbol{Q}_{RR} \end{bmatrix} \begin{bmatrix} \boldsymbol{q}_L^B \\ \boldsymbol{q}_R^A \end{bmatrix}. \tag{21}$$

Furthermore,

$$\begin{aligned} \boldsymbol{f}_L^B &= \left[\boldsymbol{D}_{LL}^B - \boldsymbol{D}_{LR}^B\left(\boldsymbol{D}_{RR}^B + \boldsymbol{D}_{LL}^A\right)^{-1}\boldsymbol{D}_{LR}^B\right]\boldsymbol{q}_{LL}^B - \boldsymbol{D}_{LR}^B\left(\boldsymbol{D}_{RR}^B + \boldsymbol{D}_{LL}^A\right)^{-1}\boldsymbol{D}_{LR}^A\boldsymbol{q}_{RR}^A, \\ \boldsymbol{f}_R^A &= -\boldsymbol{D}_{LR}^A\left(\boldsymbol{D}_{RR}^B + \boldsymbol{D}_{LL}^A\right)^{-1}\boldsymbol{D}_{LR}^B\boldsymbol{q}_{LL}^B + \left[\boldsymbol{D}_{RR}^A - \boldsymbol{D}_{LR}^A\left(\boldsymbol{D}_{RR}^B + \boldsymbol{D}_{LL}^A\right)^{-1}\boldsymbol{D}_{LR}^A\right]\boldsymbol{q}_{RR}^A, \end{aligned}$$

where $\boldsymbol{Q} = \begin{bmatrix} \boldsymbol{Q}_{LL} & \boldsymbol{Q}_{LR} \\ \boldsymbol{Q}_{RL} & \boldsymbol{Q}_{RR} \end{bmatrix}$ is the dynamic stiffness matrix for each unit cell with

$$\begin{aligned} \boldsymbol{Q}_{LL} &= \boldsymbol{U}_{LL} - \boldsymbol{U}_{LR}\left(\boldsymbol{U}_{RR} + \boldsymbol{D}_{LL}^B\right)^{-1}\boldsymbol{U}_{RL}, \\ \boldsymbol{Q}_{LR} &= -\boldsymbol{U}_{LR}\left(\boldsymbol{U}_{RR} + \boldsymbol{D}_{LL}^B\right)^{-1}\boldsymbol{D}_{LR}^B, \\ \boldsymbol{Q}_{RL} &= -\boldsymbol{D}_{RL}^A\left(\boldsymbol{U}_{RR} + \boldsymbol{D}_{LL}^B\right)^{-1}\boldsymbol{U}_{RL}, \\ \boldsymbol{Q}_{RR} &= \boldsymbol{D}_{RR}^B - \boldsymbol{D}_{RL}^B\left(\boldsymbol{U}_{RR} + \boldsymbol{D}_{LL}^B\right)^{-1}\boldsymbol{D}_{LR}^B, \end{aligned} \tag{22}$$

$$\begin{aligned} \boldsymbol{U}_{LL} &= \boldsymbol{D}_{LL}^B - \boldsymbol{D}_{LR}^B\left(\boldsymbol{D}_{RR}^B + \boldsymbol{D}_{LL}^A\right)^{-1}\boldsymbol{D}_{RL}^A, \\ \boldsymbol{U}_{LR} &= -\boldsymbol{D}_{LR}^B\left(\boldsymbol{D}_{RR}^B + \boldsymbol{D}_{LL}^A\right)^{-1}\boldsymbol{D}_{LR}^A, \\ \boldsymbol{U}_{RL} &= -\boldsymbol{D}_{RL}^A\left(\boldsymbol{D}_{RR}^B + \boldsymbol{D}_{LL}^A\right)^{-1}\boldsymbol{D}_{RL}^B, \\ \boldsymbol{U}_{RR} &= \boldsymbol{D}_{RR}^A - \boldsymbol{D}_{RL}^A\left(\boldsymbol{D}_{RR}^B + \boldsymbol{D}_{LL}^A\right)^{-1}\boldsymbol{D}_{LR}^A. \end{aligned} \tag{23}$$

Using the expressions above and applying the continuity condition $\boldsymbol{f}_R^B = -\boldsymbol{f}_L^A$, $\boldsymbol{q}_R^B = \boldsymbol{q}_L^A$ at the interface between beams A and B, and further applying the Floquet–Bloch periodicity condition, the physical parameters at both ends of the unit cell become

$$\boldsymbol{q}_R^A = e^{ik}\boldsymbol{q}_L^B, \quad \boldsymbol{f}_R^A = -e^{ik}\boldsymbol{f}_L^B, \tag{24}$$

where k designates the dimensionless Bloch parameter. Combining (21) and (24) gives

$$\begin{aligned} \left[e^{2ik} - \boldsymbol{Q}_{LR}^{-1}\boldsymbol{Q}_{RR}e^{ik} + e^{ik}\boldsymbol{Q}_{LR}^{-1}\boldsymbol{Q}_{LL} - \boldsymbol{Q}_{LR}^{-1}\boldsymbol{Q}_{RL}\right]\boldsymbol{q}_{LL}^B = \boldsymbol{0}, \\ e^{2ik}\boldsymbol{q}_{LL}^B + e^{ik}\boldsymbol{Q}_{LR}^{-1}\left[\boldsymbol{Q}_{LL} + \boldsymbol{Q}_{RR}\right]\boldsymbol{q}_{LL}^B + \boldsymbol{Q}_{LR}^{-1}\boldsymbol{Q}_{RL}\boldsymbol{q}_{LL}^B = \boldsymbol{0}. \end{aligned} \tag{25}$$

By further modification, (25) can be reexpressed as follows [Zhou et al. 2019b]:

$$\begin{aligned} \begin{bmatrix} \boldsymbol{0} & \boldsymbol{I} \\ \boldsymbol{Q}_{LR}^{-1}\boldsymbol{Q}_{RL} & \boldsymbol{Q}_{LR}^{-1}(\boldsymbol{Q}_{RR} - \boldsymbol{Q}_{LL}) \end{bmatrix}\begin{pmatrix} \boldsymbol{q}_L^B \\ e^{ik}\boldsymbol{q}_L^B \end{pmatrix} - e^{ik}\begin{pmatrix} \boldsymbol{q}_L^B \\ e^{ik}\boldsymbol{q}_L^B \end{pmatrix} = \boldsymbol{0}, \\ \begin{bmatrix} \boldsymbol{0} & \boldsymbol{I} \\ -\boldsymbol{Q}_{LR}^{-1}\boldsymbol{Q}_{RL} & -\boldsymbol{Q}_{LR}^{-1}(\boldsymbol{Q}_{LL}+\boldsymbol{Q}_{RR}) \end{bmatrix}\begin{pmatrix} \boldsymbol{q}_L^B \\ e^{ik}\boldsymbol{q}_L^B \end{pmatrix} - e^{ik}\begin{pmatrix} \boldsymbol{q}_L^B \\ e^{ik}\boldsymbol{q}_L^B \end{pmatrix} = \boldsymbol{0}, \end{aligned} \tag{26}$$

where $\boldsymbol{I}$ is the 2×2 identity matrix. This is the generalized eigenvalue problem for dispersion relation. The solution of (26) yields four roots of e^{ik} for a specific value of the normalized frequency $\overline{\omega}$. If the complex root is $x+iy$ and the associated Bloch parameter k is $p+iq$, with x, y, p, q being real, according to [Han et al. 2012; Muhammad et al. 2019] the expression $x+iy$ can be written in the form of p and q as

$$q = -\ln(x^2+y^2), \tag{27}$$

$$p = \begin{cases} \arctan(y/x) & \text{if } x > 0, \\ \pi + \arctan(y/x) & \text{if } x < 0 \text{ and } y > 0, \\ -\pi + \arctan(y/x) & \text{if } x < 0 \text{ and } y < 0. \end{cases} \tag{28}$$

Next, we consider the propagation of flexural waves in finite number of unit cells as shown in Figure 1. An excitation force is applied at the left (right) end and the output response in the form of out-of-plane displacement is received at the right (left) end. The wave motion in finite length PnC can be described by expressing the global stiffness matrix as follows [Zhou et al. 2019b]:

$$\boldsymbol{f}_{\text{tot}} = \boldsymbol{Q}_{\text{tot}}\, \boldsymbol{q}_{\text{tot}}. \tag{29}$$

Here $\boldsymbol{f}_{\text{tot}}$, $\boldsymbol{q}_{\text{tot}}$ and $\boldsymbol{Q}_{\text{tot}}$ are global force, displacement and stiffness matrix respectively. In the case of an excitation signal induced at the left end of finite length PnCs and the out-of-plane displacement is recorded at the right end, the force, displacement and stiffness vectors are

$$\boldsymbol{q}_{\text{tot}} = \begin{Bmatrix} \boldsymbol{q}_{(0)} \\ \boldsymbol{q}_{(1)} \\ \vdots \\ \boldsymbol{q}_{(N)} \end{Bmatrix}, \quad \boldsymbol{f}_{\text{tot}} = \begin{Bmatrix} \boldsymbol{f}_{(0)} \\ \boldsymbol{0} \\ \vdots \\ \boldsymbol{0} \end{Bmatrix}, \quad \boldsymbol{f}_{(0)} = \begin{pmatrix} \bar{P}_I \\ 0 \end{pmatrix}, \quad \boldsymbol{q}_{(0)} = \begin{pmatrix} \bar{w}_I \\ \bar{\psi}_I \end{pmatrix}, \quad \boldsymbol{q}_{(N)} = \begin{pmatrix} \bar{w}_O \\ \bar{\psi}_O \end{pmatrix}, \tag{30}$$

$$\boldsymbol{Q}_{\text{tot}} = \begin{bmatrix} \boldsymbol{Q}_{(1)}^{LL} & \boldsymbol{Q}_{(1)}^{LR} & \boldsymbol{0} & \boldsymbol{0} & \cdots & \boldsymbol{0} & \boldsymbol{0} \\ \boldsymbol{Q}_{(1)}^{RL} & \boldsymbol{Q}_{(1)}^{RR} + \boldsymbol{Q}_{(2)}^{LL} & \boldsymbol{Q}_{(2)}^{LR} & \boldsymbol{0} & \vdots & \vdots & \boldsymbol{0} \\ \boldsymbol{0} & \boldsymbol{Q}_{(2)}^{RL} & \boldsymbol{Q}_{(2)}^{RR} + \boldsymbol{Q}_{(3)}^{LL} & \cdots & \cdots & \cdots & \vdots \\ \boldsymbol{0} & \boldsymbol{0} & \vdots & \ddots & \vdots & \boldsymbol{0} & \boldsymbol{0} \\ \vdots & \cdots & \cdots & \cdots & \boldsymbol{Q}_{(N-2)}^{RR} + \boldsymbol{Q}_{(N-1)}^{LL} & \boldsymbol{Q}_{(N-1)}^{LR} & \boldsymbol{0} \\ \boldsymbol{0} & \cdots & \ddots & \boldsymbol{0} & \boldsymbol{Q}_{(N-1)}^{RL} & \boldsymbol{Q}_{(N-1)}^{RR} + \boldsymbol{Q}_{(N)}^{LL} & \boldsymbol{Q}_{(N)}^{LR} \\ \boldsymbol{0} & \boldsymbol{0} & \boldsymbol{0} & \boldsymbol{0} & \boldsymbol{0} & \boldsymbol{Q}_{(N)}^{RL} & \boldsymbol{Q}_{(N)}^{RR} \end{bmatrix}. \tag{31}$$

The wave transmission ratio can be expressed as

$$FRF = 20 \log \frac{\bar{w}_0}{\bar{w}_I}, \tag{32}$$

where w_0 and w_I are the out-of-plane displacement at the output and input end of the finite length PnCs.

3.2. ***Longitudinal waves.*** Now we consider the propagation of longitudinal waves in an infinite PnC. The longitudinal wave propagation can be expressed by [Muhammad et al. 2019]

$$\rho \frac{\partial^2 u}{\partial t^2} = \frac{\partial}{\partial x}\left(E \frac{\partial u}{\partial x}\right), \tag{33}$$

where $\rho$and E are mass density and Young's modulus. The displacement in the n-th unit cell can be expressed written as

$$u_n^s(x,t) = U_n^{(s)} e^{i\omega t} = \left[A_n^{(s)+} e^{ikx} + A_n^{(s)-} e^{-ikx}\right] e^{i\omega t}. \tag{34}$$

By considering continuity of displacement and stress at the interface of topologically distinct PnCs and periodicity condition $U_{n+1}^{(s)}(x+h) = U_n^{(s)}(x) e^{ik\bar{L}}$, the unknown coefficients $\{A_n^{(1)+}, A_n^{(1)-}, A_n^{(2)+}, A_n^{(2)-}\}$ can be determined by

$$\begin{bmatrix} 1 & -1 & 1 & -1 \\ \frac{\omega}{c_{L_B}}\frac{Z_B^2}{\rho_B} & -\frac{\omega}{c_{L_A}}\frac{Z_A^2}{\rho_A} & -\frac{\omega}{c_{L_B}}\frac{Z_B^2}{\rho_B} & \frac{\omega}{c_{L_A}}\frac{Z_A^2}{\rho_A} \\ e^{i\left(kL-\frac{\omega}{c_{L_B}}L_B\right)} & -e^{i\frac{\omega}{c_{L_A}}L_A} & e^{i\left(kL+\frac{\omega}{c_{L_B}}L_B\right)} & -e^{-i\frac{\omega}{c_{L_A}}L_A} \\ \frac{\omega}{c_{L_B}}\frac{Z_B^2}{\rho_B} e^{i\left(kL-k_1L_B\right)} & -\frac{\omega}{c_{L_A}}\frac{Z_A^2}{\rho_A} e^{i\frac{\omega}{c_{L_A}}L_A} & -\frac{\omega}{c_{L_B}}\frac{Z_B^2}{\rho_B} e^{i\left(kL+\frac{\omega}{c_{L_B}}L_B\right)} & \frac{\omega}{c_{L_A}}\frac{Z_A^2}{\rho_A} e^{-i\frac{\omega}{c_{L_A}}L_A} \end{bmatrix} \begin{Bmatrix} A_n^{(1)+} \\ A_n^{(1)-} \\ A_n^{(2)+} \\ A_n^{(2)-} \end{Bmatrix} = 0, \tag{35}$$

where $Z = \rho c_L$ is the impedance, k is the wavenumber and c_L is the longitudinal wave velocity. Superscript A, B designate quantities for corresponding beams. From (35) the constitutive equation for the dispersion relation can be computed as

$$\cos(kL) = \cos\frac{2\omega L_B}{c_L}\cos\frac{\omega L_A}{c_L} - \frac{1}{2}\left(\frac{S_A}{S_B} + \frac{S_B}{S_A}\right)\sin\frac{2\omega L_B}{c_L}\sin\frac{\omega L_A}{c_L}. \tag{36}$$

Substituting $L = L_A + 2L_B$ leads to

$$\cos(k\bar{L}) = \cos(\frac{\overline{\omega}\bar{L}}{c_L}) - 0.5\left(\frac{\bar{S}_A}{\bar{S}_B} + \frac{\bar{S}_B}{\bar{S}_A} - 2\right)\sin\frac{2\overline{\omega}\bar{L}_B}{c_L}\sin\frac{\overline{\omega}\bar{L}_A}{c_L}, \tag{37}$$

which is the dispersion relation for longitudinal waves. For each ω, the wavenumber k can be determined accordingly.

The propagation of longitudinal waves in a finite length PnCs as shown in Figure 1(c-d) is further considered. The wave motion for a finite PnC can be expressed by the global stiffness matrix as

$$\boldsymbol{f}_{\text{tot}} = \boldsymbol{D}_{\text{tot}}\,\boldsymbol{q}_{\text{tot}}, \tag{38}$$

where $\boldsymbol{D}_{\text{tot}} = \boldsymbol{K} - \boldsymbol{M}\overline{\omega}^2$ is the dynamic stiffness matrix with $\boldsymbol{K}$ and $\boldsymbol{M}$ being the global stiffness and mass matrix, respectively. Besides, $\boldsymbol{f}_{\text{tot}}$ and $\boldsymbol{q}_{\text{tot}}$ are vectors of the global nodal force and displacement,

respectively, given by

$$\boldsymbol{q}_{\text{tot}} = \begin{Bmatrix} \boldsymbol{q}_{(0)} \\ \boldsymbol{q}_{(1)} \\ \vdots \\ \boldsymbol{q}_{(N)} \end{Bmatrix}, \quad \boldsymbol{f}_{\text{tot}} = \begin{Bmatrix} \boldsymbol{f}_{(0)} \\ \boldsymbol{0} \\ \vdots \\ \boldsymbol{0} \end{Bmatrix}, \quad \boldsymbol{f}_{(0)} = \begin{pmatrix} \bar{P}_I \\ 0 \end{pmatrix}, \quad \boldsymbol{q}_{(0)} = (\bar{u}_I), \quad \boldsymbol{q}_{(N)} = (\bar{u}_O), \tag{39}$$

$$\boldsymbol{D}_{\text{tot}} = \begin{bmatrix} \boldsymbol{D}_{(1)}^{LL} & \boldsymbol{D}_{(1)}^{LR} & \boldsymbol{0} & \boldsymbol{0} & \cdots & \boldsymbol{0} & \boldsymbol{0} \\ \boldsymbol{D}_{(1)}^{RL} & \boldsymbol{D}_{(1)}^{RR} + \boldsymbol{D}_{(2)}^{LL} & \boldsymbol{D}_{(2)}^{LR} & \boldsymbol{0} & \vdots & \vdots & \boldsymbol{0} \\ \boldsymbol{0} & \boldsymbol{D}_{(2)}^{RL} & \boldsymbol{D}_{(2)}^{RR} + \boldsymbol{D}_{(3)}^{LL} & \cdots & \cdots & \cdots & \vdots \\ \boldsymbol{0} & \boldsymbol{0} & \vdots & \ddots & \vdots & \boldsymbol{0} & \boldsymbol{0} \\ \vdots & \cdots & \cdots & \cdots & \boldsymbol{D}_{(N-2)}^{RR} + \boldsymbol{D}_{(N-1)}^{LL} & \boldsymbol{D}_{(N-1)}^{LR} & \boldsymbol{0} \\ \boldsymbol{0} & \cdots & \ddots & \boldsymbol{0} & \boldsymbol{D}_{(N-1)}^{RL} & \boldsymbol{D}_{(N-1)}^{RR} + \boldsymbol{D}_{(N)}^{LL} & \boldsymbol{D}_{(N)}^{LR} \\ \boldsymbol{0} & \boldsymbol{0} & \boldsymbol{0} & \boldsymbol{0} & \boldsymbol{0} & \boldsymbol{D}_{(N)}^{RL} & \boldsymbol{D}_{(N)}^{RR} \end{bmatrix}. \tag{40}$$

The wave transmission ratio can be expressed as

$$FRF = 20 \log \frac{\bar{u}_0}{\bar{u}_I}, \tag{41}$$

where u_0 and u_I are the displacements at the input and output ends.

4. Phononic crystal geometric phases

Pancharatnam [1956] introduced the idea of geometric phases while investigating light propagation through a sequence of polarizers. The study was latter extended to quantum mechanics in [Berry 1984]. See [Ma et al. 2019] for a detailed review of geometric phase in acoustic and mechanical lattices. The intersection of two bands at the Weyl point [Young et al. 2012] in a 3D system results in the variation of geometric phases. The Weyl point can be regarded as a source/drain of Berry flux, which is the surface integral of Berry curvature enhanced topological charge. For a 2D system, the Chern number is used to indicate the surface integral [Aidelsburger et al. 2014]. For a 1D model, the Zak phase is an integration of Berry connection [Ma et al. 2019]. Multiple studies have explained this characterization through the Su–Schrieffer–Heeger (SSH) model for acoustic and electronic system [Chiang et al. 1977; Li et al. 2018]. There are multiple studies [Chiang et al. 1977; Mei et al. 2016; Su et al. 1979] on the energy bandgap by electrons staggered hopping at the joint of unit cell. For a 1D system, the closing and reopening of bandgap depend upon the strength of intercell and intracell hopping. The topological nontrivial phase is induced when intercell hopping is stronger than intracell hopping. Stronger intracell hopping results in trivial topological phases. The interface mode is induced for lattices with nontrivial topological phases.

Apart from the SSH model, the similar concept can be applied in PnCs. The hopping strength can be controlled by adjusting the cross-sectional area of the unit cell. Variation in the cross-section of the unit cell lattice reveals band closing and reopening with an exchange of geometric phases determined by the Zak phase. The geometric phases of the bulk band are determined by integrating the Berry connection

over the Brillouin zone [Ma et al. 2019]. Due to inversion symmetry of the unit cell, the Zak phase has a quantized value of 0 or π. For a bulk band with $\theta_n^{\text{Zak}} = 0$, the symmetry at the center and edge of the Brillouin zone remains unchanged however for a bulk band with $\theta_n^{\text{Zak}} = \pi$, the symmetry of the edge mode at the center and edge of the Brillouin zone varies and it results in an antisymmetric edge mode.

As reported in [Li et al. 2018; Xiao et al. 2015; Zhao et al. 2018] for acoustic media and in [Muhammad et al. 2019; Yin et al. 2018; Zhou et al. 2019b] for elastic media, geometric phases provide important information about the symmetry characteristic of the edge states. The transition in the symmetry type of band edge for a topological PnCs results in the generation of an interface mode. If two PnCs with different topological properties (symmetric and antisymmetric edge states) are combined and the mode transition frequency is common between their bandgaps, an interface mode with robust energy field at the boundary of PnCs are induced. Thus, the knowledge of geometric phases is important for achieving a TPIM. Although the Zak phase has been extensively studied in the acoustic system in theory and experiment [Xiao et al. 2015], in this study the method reported by [Xiao et al. 2015] is adopted to numerically determine the Zak phase of the Bloch bands in elastic media.

The geometric phase of the n-th Bloch band in a 1D system can be expressed as

$$\theta_n^{\text{Zak}} = \int_{-\pi/a}^{\pi/a} \left[i \int_{\substack{\text{unit} \\ \text{cell}}} \frac{1}{2\rho c^2} dx \xi_{n,k}^*(x) \partial \xi_{n,k}(x) \right] dk, \tag{42}$$

where $\xi_{n,k}(x)$ is the Bloch eigenstate function of the periodic structure for a specific wavenumber k and $1/\left(2\rho c^2\right)$ is the factor for weight function of elastic medium. The Bloch eigenstate function in the n-th Bloch band is given by [Xiao et al. 2015]

$$U_{n,k}(x) \text{ or } W_{n,k}(x) = \xi_{n,k}(x) e^{ikx}. \tag{43}$$

Here $U_{n,k}(x)$ and $W_{n,k}(x)$ denote the longitudinal and flexural modes, respectively. COMSOL Multiphysics is used to discretize (43) and determine the Zak phase [Xiao et al. 2015], using

$$\theta_n^{\text{Zak}} = -\text{Im} \sum_{i=1}^{N} \ln \left[\int_{\substack{\text{unit} \\ \text{cell}}} \frac{1}{2\rho c^2} dx \xi_{n,k_i}^*(x) \partial \xi_{n,k_{i+1}}(x) \right]. \tag{44}$$

5. Result analysis and discussion

5.1. ***Flexural waves.*** To verify the validity and accuracy of this theoretical model, a COMSOL based numerical simulation study is conducted for the finite (frequency response) and infinite (band structure) models. For flexural waves, TB1 ($\delta = -0.9$), TB2 ($\delta = -0.71$) and TB3 ($\delta = -0.38$) are considered with band structure shown in Figure 3. For the first three Bloch bands, the geometric phases for the lower and higher edges of the second bandgap is determined. The geometric phase of the second Bloch band for TB1 is symmetric while for TB3 it is antisymmetric with respect to the central cross-sectional plane. The band inversion for TB2 is shown in Figure 3(b). The center and edge vibration modes of the Brillouin zone are shown at the inset of Figure 3. For TB1 since the center (yellow) and edge (red) vibration mode of Brillouin zone is symmetric with respect to the central cross-sectional plane, the Zak phase is 0 while for TB3 it is opposite.

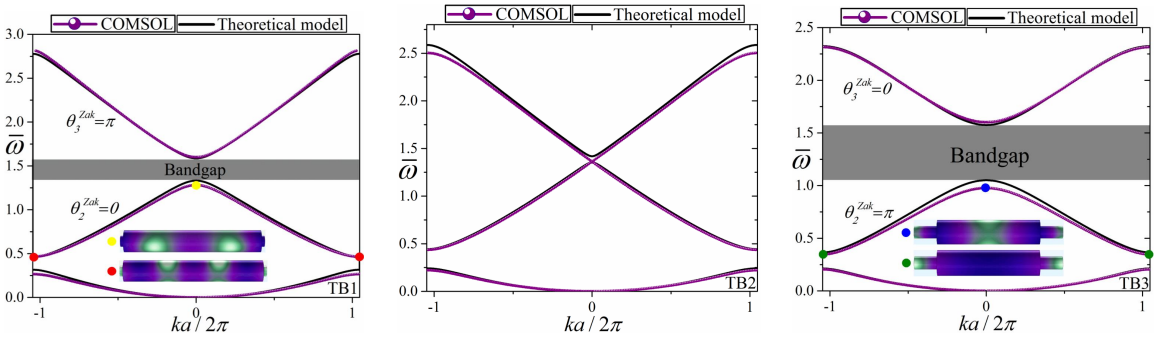

Figure 3. Flexural waves band structure with geometric phases of the band edge-state for (a) TB1, (b) TB2, and (c) TB3. An exchange in wave mode polarization with band inversion and accidental degeneracy can be observe for TB2. Mode shapes corresponding to center and edges of the Brillouin zone are shown at the inset of figures where symmetric and unsymmetric edge states can be distinguished. Solid black and dotted violet colors correspond to theoretical and numerical results, respectively.

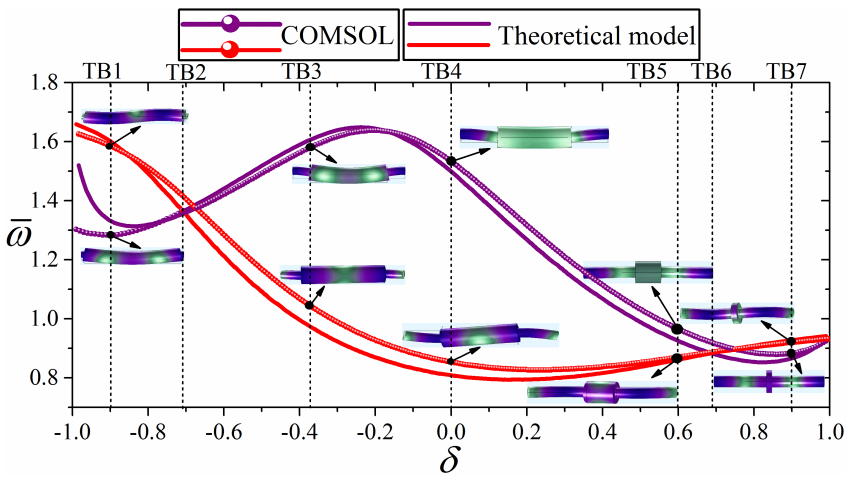

Figure 4. Dirac cone for flexural waves with bounding eigenfrequencies calculated for varying δ with band transition and accidental degeneracy point. Solid (theoretical) and dotted (numerical) red and violet colors correspond to antisymmetric and symmetric edge states, respectively. At the mode transition frequency, an exchange in wave mode polarization can be observed through the mode shapes.

Furthermore, the bounding eigenfrequencies for the second and third Bloch bands corresponding to varying δ at the center of the Brillouin zone ($k = 0$) are determined. The symmetric (purple) and antisymmetric (red) edge modes are highlighted with band inversion. An exchange in wave mode polarization is observed at TB2, the details are available in [Muhammad et al. 2019; Yin et al. 2018]. For $\delta > -0.9$, the difference in frequency for the lower edge of the second bandgap can be observed due to model dissimilarity between the spectral element method and FEM.

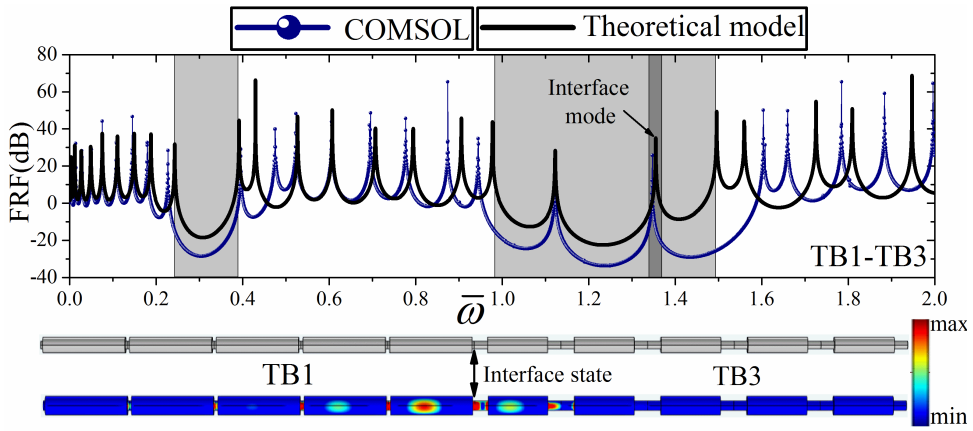

Figure 5. A finite unit cell based frequency response study with five unit cells of TB1 connecting five unit cells of TB3 with interface mode. An excitation force is applied at the left (right) end and displacement is recorded at the right (left) end. The existence of interface mode can be seen from the von Mises stress plot shown at the bottom. The interface mode frequency (black arrow) is identical to the mode transition frequency in Figure 4.

We consider ten unit cells of TB1-TB3 to analyze the presence and significance of TPIM. An excitation signal is applied at the left (right) end of the finite length model and out-of-plane displacement is recorded at the right (left) end. Since the mode transition frequency is common between the bandgaps of TB1-TB3 (Figure 4), an interface mode is generated as shown in Figure 5. The simple and von Mises stress figure of finite length PnCs with interface mode are shown for reference. From the von Mises stress figure, localization and confinement of wave energy at the interface of TB1-TB3 can be observed. The interface mode corresponds to mode transition frequency where an exchange in wave mode polarization occurs (see Figure 4), thus the accuracy of the finite unit cell model developed in this study is validated.

Furthermore, we also consider ten unit cells of TB1-TB3, TB1-TB4 and TB5-TB7 separately to further corroborate the claim for TPIM generation. As shown in Figure 6, for TB1-TB4 and TB5-TB7, no interface mode is obtained because the mode transition frequency is not common between the bandgaps of topologically distinct PnCs. Thus, it validates the statement that an interface state is induced when PnCs are topologically distinct and mode transition frequency is common between the bandgaps.

5.2. ***Longitudinal waves.*** In this section, we consider longitudinal wave propagation in topologically distinct PnCs shown in Figure 1. The response of the band inversion for TL2 ($\delta = 0$), band structures for TL1 ($\delta = -1/3$) and TL3 ($\delta = 1/3$) is presented in Figure 7. The geometric phases of the Block bands at the lower and upper edge of the bandgap are highlighted. For TL1 the edge state at the center and edges of the Brillouin zone is symmetric with respect to the center cross-sectional plane $\theta_2^{\text{Zak}} = 0$ while for TL3 it is antisymmetric $\theta_2^{\text{Zak}} = \pi$ where the bandgap closing and reopening can be observed for TL2. This conclusion is further confirmed by the vibration modes shown at the inset of the figures.

The symmetry characteristics of the bounding edge states are determined by scanning the geometric parameter δ at the center of the Brillouin zone ($k = 0$) as shown in Figure 8. Through the theoretical and

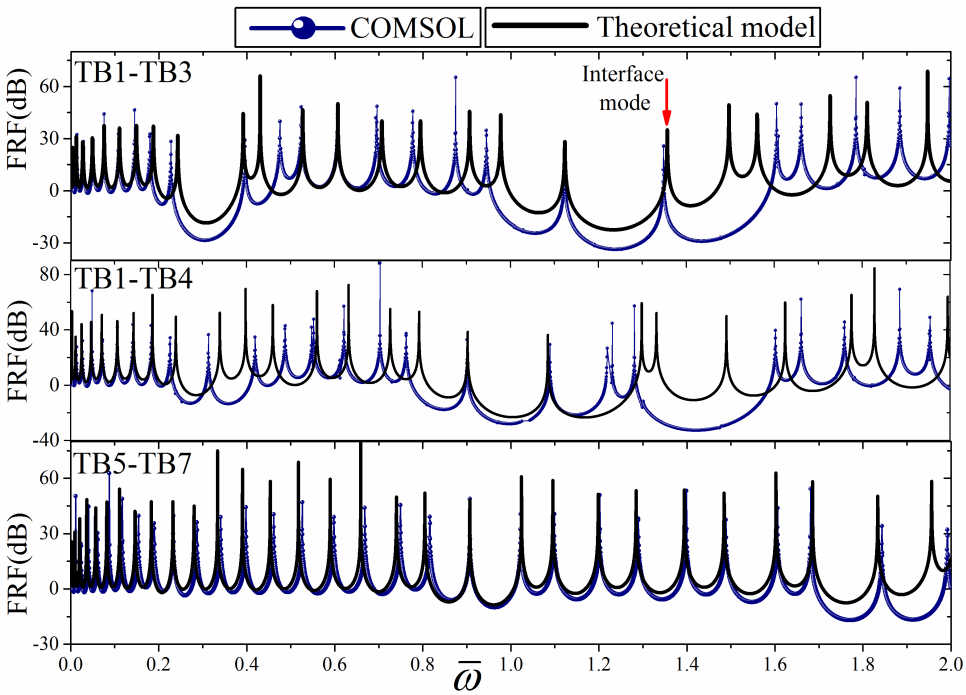

Figure 6. A finite unit cell based frequency response study. (a) Five unit cells of TB1 are connected with five cells of TB3 and the interface mode is shown with red arrow. (b) Similarly, five unit cells of TB1 are connected with five unit cells of TB4. (c) Five unit cells of TB5 are connected with five unit cells of TB7. For (b,c) no interface mode is observed as the mode transition frequency is not common between the bandgaps.

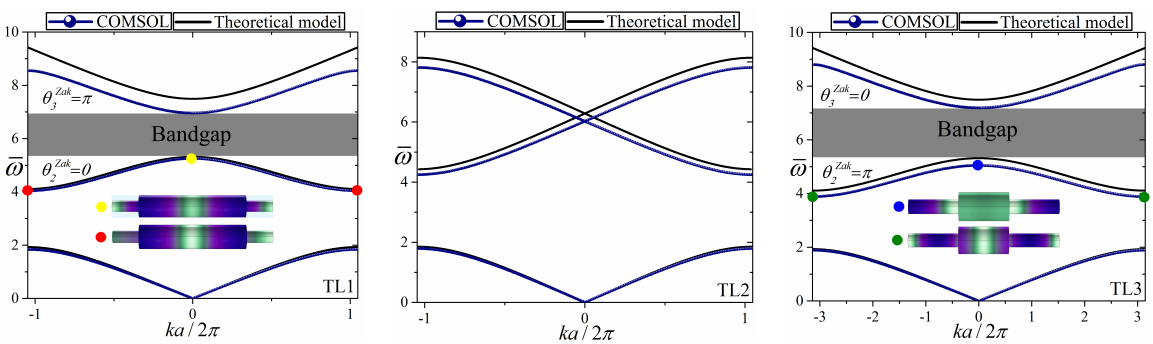

Figure 7. Longitudinal waves band structure of topologically distinct PnCs with (a) TL1 (b) TL2 (c) TL3 with geometric phases determined by the Zak phase analysis. An exchange in wave mode polarization with band inversion and accidental degeneracy can be observed for TL2. Mode shapes corresponding to center and edges of the Brillouin zone are shown at the inset of figures where symmetric and unsymmetric edge-mode states can be distinguished. Solid black and dotted violet colors correspond to theoretical and numerical solutions, respectively.

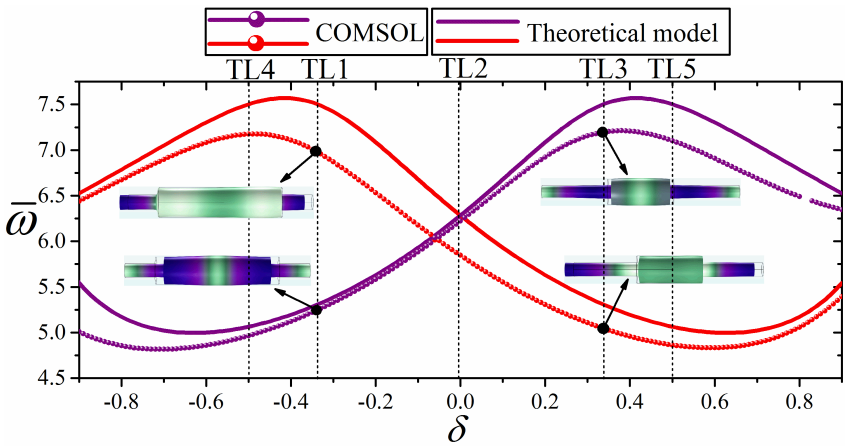

Figure 8. Longitudinal waves Dirac cone plot with bounding eigenfrequencies determined for varying δ with band transition and accidental degeneracy point. Solid (theoretical) and dotted (numerical) red and violet colors correspond to unsymmetric and symmetric edge-mode states, respectively. At the mode transition frequency, an exchange in wave mode polarization can be observed through the mode shapes shown.

numerical approaches developed here, the symmetric (purple) and antisymmetric (red) edge modes are successfully distinguished. For varying δ, the transition in the geometric phases and band inversion can be observed at TL2 where an exchange in the wave mode polarization occurs. Because longitudinal wave propagation is linearly dispersive in nature [Muhammad et al. 2019; Yin et al. 2018], thus comparing to flexural waves, a combination of any δ smaller or greater than 0 can induce an interface state, see Figure 10 for more details.

The result of an infinite unit cell model is validated by considering five unit cells of TL1 and TL3 connected together. A harmonic excitation force is applied at the left (right) end of the finite length PnCs and the displacement as output is recorded at the right (left) end. As shown in the Dirac cone plot (see Figure 8), the mode transition frequency is common between the bandgaps of TL1-TL3, thus the interface state exists. The frequency response study validates and reveals the existence of an interface mode as shown in Figure 9. The mode transition frequency reported in the Dirac cone plot is identical to the interface state frequency obtained from the theoretical and numerical models.

Similarly to Figure 6, an analysis by varying the geometric parameter array of unit cells to validate the existence of interface mode is attempted. For longitudinal wave, as demonstrated in Figure 8, any two geometric configurations with a mode transition frequency common between the bandgaps of topological distinct PnCs, can induce an interface state. In Figure 10, it shows the generation of an interface mode resulting from ten unit cells of TL1-TL3 and TL4-TL5. The interface mode is highlighted with black arrow. Both theoretical and numerical findings further validate the conclusion for TPIM.

The spatial distribution of the displacement field at the interface mode frequency for longitudinal and bending elastic waves is shown in Figure 11. At the boundary of topological PnCs ($x = 0$), the displacement is maximum and away from it, the wave energy decays. A similar conclusion can be observed from the von Mises stress plot shown in Figure 5 and Figure 9.

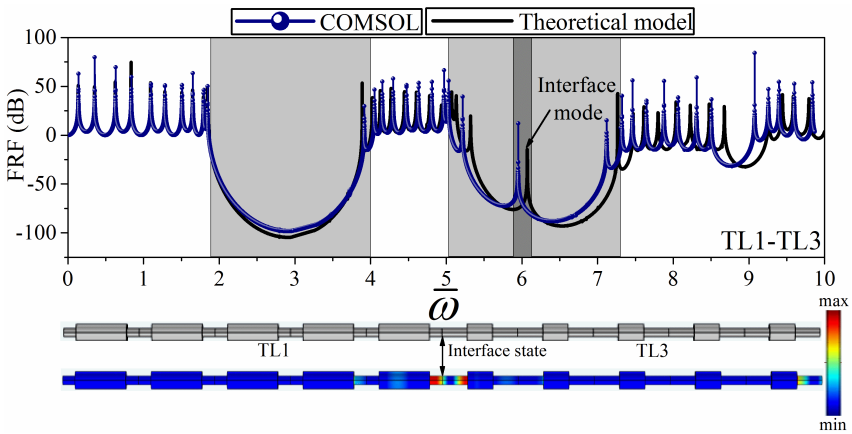

Figure 9. A finite unit cell based frequency response study with five unit cells of TL1 connecting five cells of TL3 with interface mode. An excitation force is applied at the left (right) end and displacement is recorded at the right (left) end. The existence of an interface mode can be seen from the von Mises stress plot shown at the bottom. The frequency of the interface mode is identical to the mode transition frequency in Figure 8.

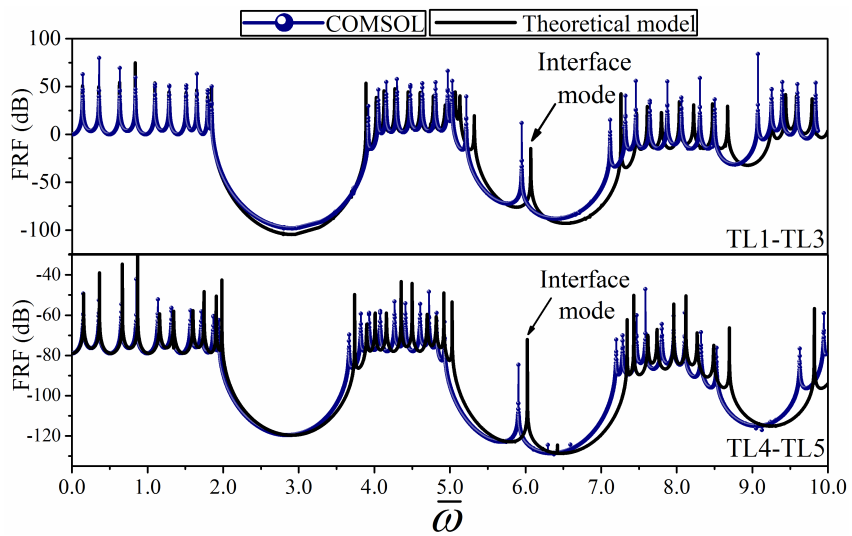

Figure 10. A finite unit cell based frequency response study. (a) Five unit cells of TL1 is connected with five unit cells of TL3. (b) Five unit cell of TL4 is connected to five unit cells of TL5. The interface state at mode transition frequency is shown with a black arrow.

6. Conclusions

In summary, a theoretical study with numerical simulation on the topological characteristics of the 1D PnC for longitudinal and bending elastic waves is presented. The interface modes are reported by spectral

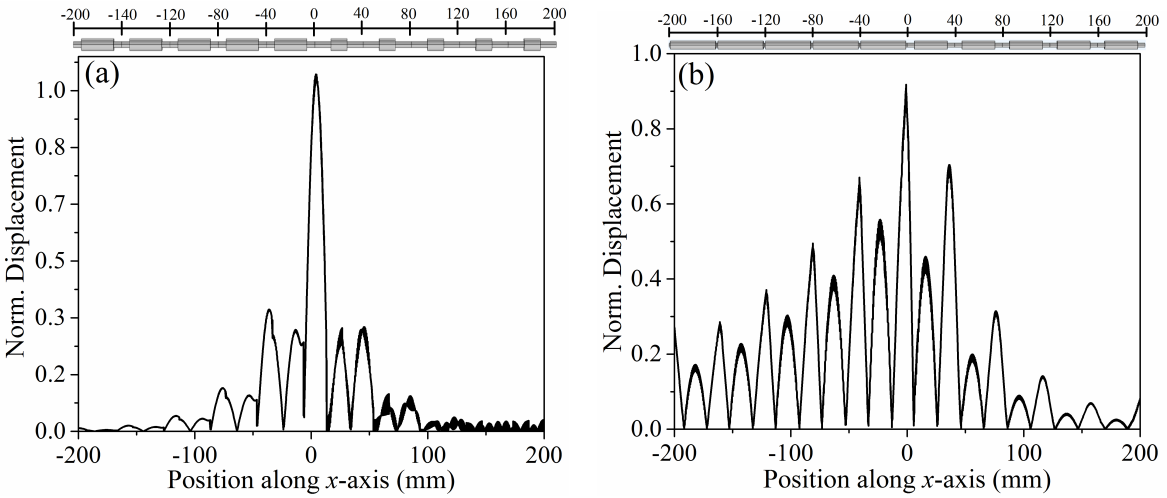

Figure 11. Spatial distribution of displacement field across the length of finite length PnC at the interface mode frequency for (a) longitudinal and (b) bending elastic waves.

element based theoretical and FEM based numerical techniques. The flexural wave dispersion relation is derived by using the Timoshenko beam model with the spectral element method. We also derived the constitutive relation for the longitudinal waves band structure with frequency response analyses. The geometric phases of the Block bands are determined by the Zak phase analysis. The symmetry characteristics of the edge modes are identified and the band inversion along with an exchange in wave mode polarization caused by topology is investigated. The Dirac cone plot for the flexural waves show distinct behavior due to nonlinear dispersive nature as compared to the longitudinal wave counterpart. The geometric phases provide useful information not only about the symmetry properties of the edge modes but also the presence of topologically protected interface modes. With the mode transition frequency being common between the bandgaps of topologically distinct PnCs, an interface mode with robust energy field at the interface with decaying energy field away from it can be observed. The robust nature, immune to backscattering and sharp edges properties of the interface mode, makes it a potential tool for solving vibration related engineering problem.

The conclusions here may contribute in the better understanding of topological phenomena of 1D PnCs. The results have been validated by comparing the theoretical and numerical solutions with excellent agreement achieved.

Acknowledgments

The work described in this paper was supported by Shenzhen Science and Technology Funding Fundamental Research Program (Project No. JCYJ20170413141248626) and General Research Grant from the Research Grants Council of the Hong Kong Special Administrative Region (Project Nos. CityU 11212017, 11216318).

List of symbols

a	lattice constant
$A_1 - A_4$	unknown constants
$\boldsymbol{B}$	unknown coefficient vector
A, B, C, D	coefficients for angular deflection, shear force and bending moments
c_L	longitudinal wave velocity
$\boldsymbol{D}$	dynamic stiffness matrix
d_B	diameter of thinner beam
D_A	diameter of thicker B
E	young's modulus
$\boldsymbol{f}$	nodal force vector
$G, \overline{G}$	shear modulus
$I_z, \bar{I}_z$	moment of inertia
$\boldsymbol{I}$	identity matrix
EI_z	flexural rigidity
k	wavenumber
$\boldsymbol{K}$	stiffness matrix
L, L_A, L_B	total length of beam with designated length for beam A-B
L/D_A	slenderness ratio
$M, \overline{M}$	bending moment
$\boldsymbol{M}$	mass matrix
P_I	input excitation force
$\boldsymbol{q}$	nodal displacement vector
$\boldsymbol{Q}$	dynamic stiffness matrix for each unit cell
$S, \bar{S}, S_A, S_B$	cross-section area
S_1, S_2, S_3	unknown coefficients
$u, \bar{u}$	in-plane displacement
$U_{n,k}$	longitudinal wave field
$V, \overline{V}$	shear force
$w, \bar{w}$	out-of-plane displacement
$W_{n,k}$	flexural wave field
$x, \bar{x}$	local coordinate
Z	impedance
0	symmetric edge mode
δ	geometric parameter
ζ_j	unknown roots
θ_n^{Zak}	Zak phase of nth Bloch band
i	iota
κ	shear correction factor
ν	poisson ratio
$\xi_{n,k}$	Bloch eigenfunction
π	antisymmetric edge mode
ρ, ρ_B	density
$\sum_{i=1}^{n}$	summation
ϕ	normalized flexure rigidity
ψ	angular rotation
$\omega, \overline{\omega}$	normalized angular frequency
$', '', '''$	first, second and third differentiation with respect to $\bar{x}$

References

[Aidelsburger et al. 2014] M. Aidelsburger, M. Lohse, C. Schweizer, M. Atala, J. T. Barreiro, S. Nascimbène, N. R. Cooper, I. Bloch, and N. Goldman, "Measuring the Chern number of Hofstadter bands with ultracold bosonic atoms", *Nature Phys.* **11** (2014), 162.

[Andrade et al. 2018] C. Andrade, C. S. Ha, and R. S. Lakes, "Extreme Cosserat elastic cube structure with large magnitude of negative Poisson's ratio", *J. Mech. Mater. Struct.* **13**:1 (2018), 93–101.

[Bernevig et al. 2006] B. A. Bernevig, T. L. Hughes, and S.-C. Zhang, "Quantum spin Hall effect and topological phase transition in HgTe quantum wells", *Science* **314** (2006), 1757–1761.

[Berry 1984] M. V. Berry, "Quantal phase factors accompanying adiabatic changes", *Proc. Roy. Soc. London Ser. A* **392**:1802 (1984), 45–57.

[Brendel et al. 2018] C. Brendel, V. Peano, O. Painter, and F. Marquardt, "Snowflake phononic topological insulator at the nanoscale", *Phys. Rev. B* **97** (2018), art. id. 014110.

[Cha and Daraio 2018] J. Cha and C. Daraio, "Electrical tuning of elastic wave propagation in nanomechanical lattices at MHz frequencies", *Nature Nanotechnol.* **13** (2018), 1016–1020.

[Chen et al. 2018a] Chen, H., Nassar, H., Huang, and G. L., "A study of topological effects in 1D and 2D mechanical lattices", *J. Mech. Phys. Solids* **117** (2018), 22–36.

[Chen et al. 2018b] H. Chen, H. Nassar, and G. Huang, "Topological mechanics of edge waves in Kagome lattices", 2018. arXiv

[Chen et al. 2019a] Chen, Wei, Wang, Lin, Dai, and Hu-Liang, "Nonlinear free vibration of nanobeams based on nonlocal strain gradient theory with the consideration of thickness-dependent size effect", *J. Mech. Mater. Struct.* **14**:1 (2019), 119–137.

[Chen et al. 2019b] Chen, Yi, Liu, Xiaoning, Hu, and Gengkai, "Topological phase transition in mechanical honeycomb lattice", *J. Mech. Phys. Solids* **122** (2019), 54–68.

[Chiang et al. 1977] C. K. Chiang, C. R. Fincher, Y. W. Park, A. J. Heeger, H. Shirakawa, E. J. Louis, S. C. Gau, and A. G. MacDiarmid, "Electrical Conductivity in Doped Polyacetylene", *Phys. Rev. Lett.* **39** (1977), 1098–1101.

[Czubacki et al. 2015] Czubacki, R. aw, Lewiński, and Tomasz, "Topology optimization of spatial continuum structures made of nonhomogeneous material of cubic symmetry", *J. Mech. Mater. Struct.* **10**:4 (2015), 519–535.

[Delplace et al. 2011] P. Delplace, D. Ullmo, and G. Montambaux, "Zak phase and the existence of edge states in graphene", *Phys. Rev. B* **84** (2011), art. id. 195452.

[Dong et al. 2017] J. W. Dong, X. D. Chen, H. Zhu, Y. Wang, and X. Zhang, "Valley photonic crystals for control of spin and topology", *Nature Mater.* **16** (2017), 298–302.

[Foehr et al. 2018] A. Foehr, O. R. Bilal, S. D. Huber, and C. Daraio, "Spiral-based phononic plates: from wave beaming to topological insulators", *Phys. Rev. Lett.* **120** (2018), art. id. 205501.

[Gao et al. 2018] R. Z. Gao, G. Y. Zhang, T. Ioppolo, and X.-L. Gao, "Elastic wave propagation in a periodic composite beam structure: A new model for band gaps incorporating surface energy, transverse shear and rotational inertia effects", *J. Micromech. Molec. Phys.* **03** (2018), art. id. 1840005.

[Haldane 1988] F. D. Haldane, "Model for a quantum Hall effect without Landau levels: Condensed-matter realization of the 'parity anomaly'", *Phys. Rev. Lett.* **61** (1988), 2015–2018.

[Han et al. 2012] L. Han, Y. Zhang, Z. Q. Ni, Z. M. Zhang, and L. H. Jiang, "A modified transfer matrix method for the study of the bending vibration band structure in phononic crystal Euler beams", *Physica B* **407** (2012), 4579–4583.

[Hasan and Kane 2010] M. Z. Hasan and C. L. Kane, "Colloquium: Topological insulators", *Rev Mod Phys* **82** (2010), 3045–3067.

[He et al. 2016] C. He, X. Ni, H. Ge, X. C. Sun, Y. B. Chen, M. H. Lu, X. P. Liu, and Y. F. Chen, "Acoustic topological insulator and robust one-way sound transport", *Nature Phys.* **12** (2016), 1124–.

[Huber 2016] S. D. Huber, "Topological mechanics", *Nature Phys.* **12** (2016), 621–623.

[Huo et al. 2017] S. Y. Huo, J. J. Chen, H. B. Huang, and G. L. Huang, "Simultaneous multi-band valley-protected topological edge states of shear vertical wave in two-dimensional phononic crystals with veins", *Sci. Rep.* **7** (2017), art. id. 10335.

[Jia et al. 2018] D. Jia, H. x. Sun, J. p. Xia, S. q. Yuan, X. j. Liu, and C. Zhang, "Acoustic topological insulator by honeycomb sonic crystals with direct and indirect band gaps", *New J. Phys.* **20** (2018), art. id. 093027.

[Jin et al. 2018] Y. Jin, D. Torrent, and B. Djafari-Rouhani, "Robustness of conventional and topologically protected edge states in phononic crystal plates", *Phys. Rev. B* **98** (2018), art. id. 054307.

[Kane and Mele 2005] C. L. Kane and E. J. Mele, "Quantum spin Hall effect in graphene", *Phys. Rev. Lett.* **95** (2005), art. id. 226801.

[Khanikaev et al. 2013] A. B. Khanikaev, S. H. Mousavi, W. K. Tse, M. Kargarian, A. H. MacDonald, and G. Shvets, "Photonic topological insulators", *Nature Mater.* **12** (2013), 233–239.

[Khanikaev et al. 2015] A. B. Khanikaev, R. Fleury, S. H. Mousavi, and A. Alù, "Topologically robust sound propagation in an angular-momentum-biased graphene-like resonator lattice", *Nature Comm.* **6** (2015), art. id. 8260.

[Kim et al. 2018] I. Kim, S. Iwamoto, and Y. Arakawa, "Topologically protected elastic waves in one-dimensional phononic crystals of continuous media", *Appl. Phys. Express* **11** (2018), art. id. 017201.

[Kushwaha et al. 1993] M. S. Kushwaha, P. Halevi, L. Dobrzynski, and B. Djafari-Rouhani, "Acoustic band structure of periodic elastic composites", *Phys. Rev. Lett.* **71** (1993), 2022–2025.

[Li et al. 2018] X. Li, Y. Meng, X. X. Wu, S. Yan, Y. Z. Huang, S. X. Wang, and W. J. Wen, "Su-Schrieffer-Heeger model inspired acoustic interface states and edge states", *Appl. Phys. Lett.* **113** (2018), art. id. 203501.

[Liu et al. 2000] Z. Liu, X. Zhang, Y. Mao, Y. Y. Zhu, Z. Yang, C. T. Chan, and P. Sheng, "Locally resonant sonic materials", *Science* **289** (2000), 1734–1736.

[Ma et al. 2019] G. Ma, M. Xiao, and C. T. Chan, "Topological phases in acoustic and mechanical systems", *Nature Rev. Phys.* **1** (2019), 281–294.

[Martínez-Sala et al. 1995] R. Martínez-Sala, J. Sancho, J. V. Sánchez, V. Gómez, J. Llinares, and F. Meseguer, "Sound attenuation by sculpture", *Nature* **378** (1995), 241–241.

[Mei et al. 2016] J. Mei, Z. Chen, and Y. Wu, "Pseudo-time-reversal symmetry and topological edge states in two-dimensional acoustic crystals", *Sci. Rep.* **6** (2016), art. id. 32752.

[Miniaci et al. 2018] M. Miniaci, R. K. Pal, B. Morvan, and M. Ruzzene, "Experimental observation of topologically protected helical edge modes in patterned elastic plates", *Phys. Rev. X* **8** (2018), art. id. 031074.

[Moore 2010] J. E. Moore, "The birth of topological insulators", *Nature* **464** (2010), 194–198.

[Muhammad et al. 2019] Muhammad, W. Zhou, and C. W. Lim, "Topological edge modeling and localization of protected interface modes in 1D phononic crystals for longitudinal and bending elastic waves", *Int. J. Mech. Sci.* **159** (2019), 359–372.

[Pal et al. 2018] R. K. Pal, J. Vila, M. Leamy, and M. Ruzzene, "Amplitude-dependent topological edge states in nonlinear phononic lattices", *Phys. Rev. E* **97** (2018), art. id. 032209.

[Pancharatnam 1956] S. Pancharatnam, "Generalized theory of interference and its applications, II: Partially coherent pencils", *Proc. Indian Acad. Sci. Sect. A* **44** (1956), 398–417.

[Reda et al. 2016] H. Reda, Y. Rahali, J. F. Ganghoffer, and H. Lakiss, "Wave propagation analysis in 2D nonlinear hexagonal periodic networks based on second order gradient nonlinear constitutive models", *Int J Nonlin Mech* **87** (2016), 85–96.

[Sigalas and Economou 1993] M. Sigalas and E. N. Economou, "Band structure of elastic waves in two dimensional systems", *Solid state communications* **86** (1993), 141–143.

[Su et al. 1979] W. P. Su, J. R. Schrieffer, and A. J. Heeger, "Solitons in polyacetylene", *Phys. Rev. Lett.* **42** (1979), 1698–1701.

[Susstrunk and Huber 2015] R. Susstrunk and S. D. Huber, "PHYSICS. Observation of phononic helical edge states in a mechanical topological insulator", *Science* **349** (2015), 47–50.

[Wang et al. 2015] P. Wang, L. Lu, and K. Bertoldi, "Topological Phononic Crystals with One-Way Elastic Edge Waves", *Phys. Rev. Let.* **115** (2015), art. id. 104302.

[Xia et al. 2018] J.-P. Xia, D. Jia, H.-X. Sun, S.-Q. Yuan, Y. Ge, Q.-R. Si, and X.-J. Liu, "Programmable coding acoustic topological insulator", *Adv. Mater.* **30** (2018), art. id. 1805002.

[Xiao et al. 2010] D. Xiao, M. C. Chang, and Q. Niu, "Berry phase effects on electronic properties", *Rev. Modern Phys.* **82**:3 (2010), 1959–2007.

[Xiao et al. 2015] M. Xiao, G. C. Ma, Z. Y. Yang, P. Sheng, Z. Q. Zhang, and C. T. Chan, "Geometric phase and band inversion in periodic acoustic systems", *Nature Phys.* **11** (2015), 240–244.

[Yin et al. 2018] J. Yin, M. Ruzzene, J. Wen, D. Yu, L. Cai, and L. Yue, "Band transition and topological interface modes in 1D elastic phononic crystals", *Sci. Rep.* **8** (2018), art. id. 6806.

[Young et al. 2012] S. M. Young, S. Zaheer, J. Y. Teo, C. L. Kane, E. J. Mele, and A. M. Rappe, "Dirac semimetal in three dimensions", *Phys. Rev. Lett.* **108** (2012), art. id. 140405.

[Yu et al. 2006] D. Yu, Y. Liu, G. Wang, H. Zhao, and J. Qiu, "Flexural vibration band gaps in Timoshenko beams with locally resonant structures", *J. Appl. Phys.* **100** (2006), art. id. 124901.

[Yu et al. 2018] S. Y. Yu, C. He, Z. Wang, F. K. Liu, X. C. Sun, Z. Li, H. Z. Lu, M. H. Lu, X. P. Liu, and Y. F. Chen, "Elastic pseudospin transport for integratable topological phononic circuits", *Nature Comm.* **9** (2018), art. id. 3072.

[Zhang et al. 2013] F. Zhang, A. H. MacDonald, and E. J. Mele, "Valley Chern numbers and boundary modes in gapped bilayer graphene", *Proc. Natl. Acad. Sci. USA* **110** (2013), 10546–10551.

[Zhang et al. 2019] Q. Zhang, Y. Chen, K. Zhang, and G. Hu, "Programmable elastic valley Hall insulator with tunable interface propagation routes", *Extreme Mech. Lett.* **28** (2019), 76–80.

[Zhao et al. 2018] D. G. Zhao, M. Xiao, C. W. Ling, C. T. Chan, and K. H. Fung, "Topological interface modes in local resonant acoustic systems", *Phys. Rev. B* **98** (2018), art. id. 014110.

[Zhou et al. 2019a] W. Zhou, Y. Su, Muhammad, W. Chen, and C. W. Lim, "Voltage-controlled quantum valley Hall effect in dielectric membrane-type acoustic metamaterials", *Int. J. Mech. Sci.* (online publication December 2019), art. id. 105368.

[Zhou et al. 2019b] W. J. Zhou, W. Q. Chen, Muhammad, and C. W. Lim, "Surface effect on the propagation of flexural waves in periodic nano-beam and the size-dependent topological properties", *Compos Struct* **216** (2019), 427–435.

[Zhou et al. 2019c] W. J. Zhou, B. Wu, Z. Chen, W. Chen, C. W. Lim, and J. N. Reddy, "Actively controllable topological phase transition in homogeneous piezoelectric rod system", 2019. Submitted.

Received 29 Jul 2019. Revised 7 Nov 2019. Accepted 29 Nov 2019.

MUHAMMAD: fmuhammad6-c@my.cityu.edu.hk
City University of Hong Kong Shenzhen Research Institute, Shenzhen 518057, China

C. W. LIM: bccwlim@cityu.edu.hk
Department of Architecture and Civil Engineering, Kowloon, Hong Kong SAR, China

JOURNAL OF MECHANICS OF MATERIALS AND STRUCTURES

msp.org/jomms

Founded by Charles R. Steele and Marie-Louise Steele

Cover photo: Ev Shafrir

See msp.org/jomms for submission guidelines.

JoMMS (ISSN 1559-3959) at Mathematical Sciences Publishers, 798 Evans Hall #6840, c/o University of California, Berkeley, CA 94720-3840, is published in 10 issues a year. The subscription price for 2020 is US $660/year for the electronic version, and $830/year (+$60, if shipping outside the US) for print and electronic. Subscriptions, requests for back issues, and changes of address should be sent to MSP.

JoMMS peer-review and production is managed by EditFLOW® from Mathematical Sciences Publishers.

PUBLISHED BY

mathematical sciences publishers

nonprofit scientific publishing

http://msp.org/

Journal of Mechanics of Materials and Structures

Volume 15, No. 1 January 2020